

Spectroscopic confirmation of a gravitationally lensed Lyman-break galaxy at z[C II] = 6.827 using NOEMA

S. J. Molyneux, R. Smit, D. Schaerer, R. J. Bouwens, L. Bradley, J. A. Hodge, S. N. Longmore, S. Schouws, P. van Der Werf, A. Zitrin, et al.

▶ **To cite this version:**

S. J. Molyneux, R. Smit, D. Schaerer, R. J. Bouwens, L. Bradley, et al.. Spectroscopic confirmation of a gravitationally lensed Lyman-break galaxy at z[C II] = 6.827 using NOEMA. Monthly Notices of the Royal Astronomical Society, 2022, 512, pp.535-543. 10.1093/mnras/stac557 . insu-03672015

HAL Id: insu-03672015
https://insu.hal.science/insu-03672015

Submitted on 19 Mar 2023

HAL is a multi-disciplinary open access archive for the deposit and dissemination of scientific research documents, whether they are published or not. The documents may come from teaching and research institutions in France or abroad, or from public or private research centers.

L'archive ouverte pluridisciplinaire **HAL**, est destinée au dépôt et à la diffusion de documents scientifiques de niveau recherche, publiés ou non, émanant des établissements d'enseignement et de recherche français ou étrangers, des laboratoires publics ou privés.

Monthly Notices of the ROYAL ASTRONOMICAL SOCIETY

MNRAS **512,** 535–543 (2022) https://doi.org/10.1093/mnras/stac557
Advance Access publication 2022 March 4

Spectroscopic confirmation of a gravitationally lensed Lyman-break galaxy at $z_{[\mathrm{C\,II}]} = 6.827$ using NOEMA

S. J. Molyneux [1,2★] R. Smit,[1] D. Schaerer,[3,4] R. J. Bouwens,[5] L. Bradley,[6] J. A. Hodge,[5] S. N. Longmore,[1] S. Schouws,[5] P. van der Werf,[5] A. Zitrin [7] and S. Phillips [1]

[1]*Astrophysics Research Institute, Liverpool John Moores University, 146 Brownlow Hill, Liverpool L3 5RF, UK*
[2]*European Southern Observatory, Karl-Schwarzschild-Strasse 2, D-85748 Garching, Germany*
[3]*Observatoire de Genève, Université de Genève, 51 Ch. des Mail-lettes, CH-1290 Versoix, Switzerland*
[4]*CNRS, IRAP, 14 avenue E. Belin, F-31400 Toulouse, France*
[5]*Leiden Observatory, Leiden University, NL-2300 RA Leiden, the Netherlands*
[6]*Space Telescope Science Institute, Baltimore, MD 21218, USA*
[7]*Physics Department, Ben-Gurion University of the Negev, PO Box 653, Be'er-Sheva 8410501, Israel*

Accepted 2022 February 14. Received 2022 February 4; in original form 2021 September 1

ABSTRACT

We present the spectroscopic confirmation of the brightest known gravitationally lensed Lyman-break galaxy in the Epoch of Reionization (EoR), A1703-zD1, through the detection of [C II] 158 μm at a redshift of $z = 6.8269 \pm 0.0004$. This source was selected behind the strong lensing cluster Abell 1703, with an intrinsic luminosity and a very blue *Spitzer*/Infrared Array Camera (IRAC) [3.6]–[4.5] colour, implying high equivalent width line emission of [O III] + Hβ. [C II] is reliably detected at 6.1σ cospatial with the rest-frame ultraviolet (UV) counterpart, showing similar spatial extent. Correcting for the lensing magnification, the [C II] luminosity in A1703-zD1 is broadly consistent with the local $L_{[\mathrm{C\,II}]}$–star formation rate (SFR) relation. We find a clear velocity gradient of 103 ± 22 km s^{-1} across the source that possibly indicates rotation or an ongoing merger. We furthermore present spectral scans with no detected [C II] above 4.6σ in two unlensed Lyman-break galaxies in the Extended Groth Strip (EGS)-Cosmic Assembly Near-infrared Deep Extragalactic Legacy Survey (CANDELS) field at $z \sim 6.6$–6.9. This is the first time that the Northern Extended Millimeter Array (NOEMA) has been successfully used to observe [C II] in a 'normal' star-forming galaxy at $z > 6$, and our results demonstrate its capability to complement the Atacama Large Millimeter/submillimeter Array (ALMA) in confirming galaxies in the EoR.

Key words: galaxies: evolution – galaxies: formation – galaxies: high-redshift.

1 INTRODUCTION

In the past decade hundreds of galaxies have been identified in the Epoch of Reionization (EoR), selected from their rest-frame ultraviolet (UV) light, using *Hubble Space Telescope* (*HST*) and ground-based optical/near-infrared (NIR) observatories (see Stark 2016, for a review and references therein). However, only a fraction of these sources have spectroscopic redshift determinations and we have a limited understanding of their physical properties. One reason for this is the difficulty in obtaining Lyman α (Lyα) observations at such high redshifts, due to its absorption by neutral hydrogen in the intergalactic and interstellar medium (IGM and ISM; with detected Lyα emitters possibly residing in early ionized bubbles; e.g. Jung et al. 2020; Endsley et al. 2021).

In recent years the Atacama Large Millimeter/submillimeter Array (ALMA) has transformed this field by confirming the redshifts of galaxies out to redshift $z = 9$ (e.g. Hashimoto et al. 2018; Smit et al. 2018; Tamura et al. 2019; Hodge & da Cunha 2020; Bouwens et al. 2021) and providing the first view of their dust obscured star formation (e.g. Watson et al. 2015; Laporte et al. 2017; Bowler et al. 2018; Schouws et al. 2021), the kinematics of these sources (e.g. Smit et al. 2018; Fujimoto et al. 2019; Hashimoto et al. 2019; Ginolfi et al. 2020), the cool gas traced by [C II], and highly ionized gas traced by [O III] (e.g. Maiolino et al. 2015; Inoue et al. 2016; Carniani et al. 2017; Laporte et al. 2017; Harikane et al. 2019; Hashimoto et al. 2019; Tamura et al. 2019; Bakx et al. 2020). Uncovering the physical properties of these primordial systems is fundamental to understanding the evolution of the first generation of galaxies and their role in cosmic reionization.

In particular, ALMA has demonstrated its ability to detect [C II] in UV bright galaxies that are intrinsically bright ($\sim$2–3 $\times$ L^* at $z = 7$) at $z \gtrsim 5$ (Capak et al. 2015; Willott et al. 2015; Smit et al. 2018; Matthee et al. 2019; Béthermin et al. 2020; Bouwens et al. 2021). However, much less is known about galaxies at these high redshifts that are more representative of the galaxy population as a whole ($L \leq L^*_{z=7}$). Our best insights into this fainter population are rare, apparently bright sources, which have been gravitationally lensed (Knudsen et al. 2016; Bradač et al. 2017; Fujimoto et al. 2021; Laporte et al. 2021). Despite the capability of ALMA to probe galaxies in the EoR, it has limited sky coverage in the Northern hemisphere and so interesting targets might be missed.

★ E-mail: smolyneu@eso.org

© 2022 The Author(s)
Published by Oxford University Press on behalf of Royal Astronomical Society

Downloaded from https://academic.oup.com/mnras/article/512/1/535/6542457 by guest on 19 March 2023

Recently, the Plateau de Bure Interferometer (PdBI) has been upgraded to the Northern Extended Millimeter Array (NOEMA). The upgrades have increased the number of antennae from six to 10 (with two more planned to eventually increase the total number to 12) providing more collecting power and therefore increased sensitivity to observe these fainter sources. A new correlator has also been installed (upgrading from Widex to PolyFix; Schuster et al. 2018), which can cover a larger frequency range in one set-up, enabling faster line scans. These upgrades arguably make NOEMA the most powerful interferometer in the Northern hemisphere, and therefore might play an important role in observing [C II] in galaxies at $z > 6$.

Here we report on a line search for [C II] 158 μm with NOEMA, targeting three galaxies in the Northern hemisphere at $z \sim 6.6$–6.9. The targets have been selected from a larger sample of Lyman-break galaxies, with high-precision photometric redshifts (Smit et al. 2014, 2015). A1703-zD1 is the standout target of our sample, lying behind the strong lensing cluster Abell 1703, with a magnification of ∼9 (Bradley et al. 2012). Because of its exceptional observed brightness, it has been targeted many times with previous observations attempting to observe Lyα, C IV, and C III with the Keck Observatory (Schenker et al. 2012; Stark et al. 2015; Mainali et al. 2018) and a previous attempt with PdBI (Schaerer et al. 2015) to observe [C II], however, these observations did not result in a significant detection.

In this paper, we present the successful spectroscopic confirmation of A1703-zD1 and constraints on the properties of the other two sources based on their non-detections. The plan of the paper is as follows. In Section 2, we describe the sample selection and observations. In Section 3, we discuss the method for line scanning and the findings from our scans. In Section 4, we provide the properties of the sources and comparisons to the literature, and in Section 5, we give our summary and conclusions. In this paper, we adopt a Kroupa initial mass function (IMF; Kroupa 2001). We adopt $H_0 = 70$ km s^{-1} Mpc^{-1}, $\Omega_M = 0.3$, and $\Omega_\Lambda = 0.7$ throughout. Magnitudes are quoted in the AB system (Oke & Gunn 1983).

2 SAMPLE SELECTION AND OBSERVATIONS

2.1 Target selection and properties

We obtained NOEMA observations of three sources: A1703-zD1 (Bradley et al. 2012; Smit et al. 2014), EGS-5711424617, and EGS-1952445714 (hereafter EGS-5711 and EGS-1952, respectively; Smit et al. 2015). These galaxies were initially selected with the Lyman-break technique as *HST*/F814W dropout galaxies and subsequently identified as sources with blue *Spitzer*/Infrared Array Camera (IRAC) [3.6]–[4.5] colours, implying high equivalent width [O III] + Hβ emission (Smit et al. 2014, 2015). The spectral energy distribution (SED) for each galaxy is shown in Appendix A.

We selected these targets due to their observed brightness ($m_{UV} \sim 24$–25), but also as they are representative of 'normal' star-forming galaxies [star formation rate (SFR) < 100 M$_\odot$ yr^{-1}] at $z \sim 7$, with intrinsic (corrected for lensing magnification, A1703-zD1 is magnified ∼9×) UV SFRs of 5–38 M$_\odot$ yr^{-1}. A list of some of the basic properties for all three galaxies is shown in Table 1. These same selection criteria were recently used to successfully confirm galaxies with ALMA at $z_{[C\,II]} = 6.808$–6.854 (Smit et al. 2018).

The inferred emission lines in the *Spitzer* observations reduce the probability range for the redshift such that observations can be carried out using one NOEMA set-up. For both A1703-zD1 and EGS-1952 the photometric redshifts of $6.7^{+0.2}_{-0.1}$ and $6.75^{+0.11}_{-0.10}$, respectively, are within this range. However, we note that EGS-5711 has $z_{phot} = 6.47^{+0.11}_{-0.10}$, outside of the colour selection range due to a tentative detection in the *HST*/F814W band. For the extreme emission line sources from Smit et al. (2015), systematic changes in the estimated photometric redshift ($\Delta z \sim 1$) are found when making changes to the input template set (in particular the strength of the emission line equivalent widths of the templates) used to fit the SEDs. As a result of these systematic uncertainties, we rely on the *Spitzer*/IRAC colour selection from Smit et al. (2015) to identify sources most likely in the redshift range ∼ 6.6–6.9, which includes some cases (like EGS-5711) where the z_{phot} is not within this range.

Table 1. Source properties based on previous observations.

Target ID	A1703-zD1	EGS-5711424617	EGS-1952445714
RA	13:14:59.418	14:19:57.114	14:19:19.524
Dec.	+51:50:00.84	+52:52:46.17	+52:44:57.14
z_{phot}	$6.7^{+0.2}_{-0.1}$ [a]	$6.47^{+0.11}_{-0.10}$ [b]	$6.75^{+0.11}_{-0.10}$ [b]
$m_{H_{160}}$	24.0 ± 0.1 [a]	25.1 ± 0.1 [b]	25.3 ± 0.1 [b]
M_{UV}	-20.6 ± 0.5 [c]	-21.77 ± 0.10	-21.64 ± 0.10
β_{UV}	-1.56 ± 0.32	-2.18 ± 0.36	-2.36 ± 0.43
μ	$9.0^{+0.9}_{-4.4}$ [a]	–	–

[a]Values from Bradley et al. (2012).
[b]Values from Smit et al. (2015).
[c]Values from Smit et al. (2014).

For A1703-zD1 we use a magnification value of $9.0^{+0.9}_{-4.4}$ taken from Bradley et al. (2012) calculated using the model described in Zitrin et al. 2010. The magnification error represents the extreme value obtained from the minimum and maximum magnifications obtained within 0.5 arcsec of the target and assuming $\Delta z \pm 1.0$ for the source redshift. To obtain a better handle on the systematic uncertainties in the lensing magnification, we ran two more trial models, one using a revised version of the light-traces-mass (LTM) technique and one fully parametric model. These models suggest a magnification in agreement with that of Bradley et al. (2012) within the uncertainties, though towards the lower end ($\mu \sim 4$–5). Critically, the weight of the nearby cluster galaxy (seen in the bottom of Fig. 1) is fixed according to the scaling relations, but in reality has a significant uncertainty that affects the magnification value. We therefore adopt the published magnification by Bradley et al. (2012, $\mu = 9.0^{+0.9}_{-4.4}$), as the uncertainties are broad enough to include the new magnifications from the trial models.

Throughout the paper, we report measured quantities (i.e. [C II] flux) as observed in the image plane, without a magnification correction, whereas derived physical quantities (i.e. $L_{[C\,II]}$, SFR$_{[C\,II]}$, and physical size) are corrected for the adopted lensing magnification.

2.2 NOEMA observations and data reduction

We obtained 1.2 mm observations using NOEMA in its most compact 10D configuration, with a single set-up for each of the three sources, A1703-zD1, EGS-5711, and EGS-1952, approved in program W18FC.

Observations of A1703-zD1 were taken on 2019 March 21, with 4.1 h on source, and covering the frequency range 241.45–249.08 GHz (upper side band, USB) and 225.97–233.60 GHz (lower side band, LSB), corresponding to a redshift range 6.63–6.87 and 7.14–7.41, respectively. The USB frequency range partly overlaps with PdBI observations taken in 2013 by Schaerer et al. (2015) and we combine the NOEMA and PdBI data in the *uv*-plane to obtain maximum depth over the redshift range of 6.80–6.88.

We observed EGS-5711 on 2019 April 16, April 30, and May 2 with 7.1 h on source in total. EGS-1952 was observed on 2019 April 8 and 9 and on 2019 May 2 and 3 with 8.7 h on source in total.

Downloaded from https://academic.oup.com/mnras/article/512/1/535/6542457 by guest on 19 March 2023

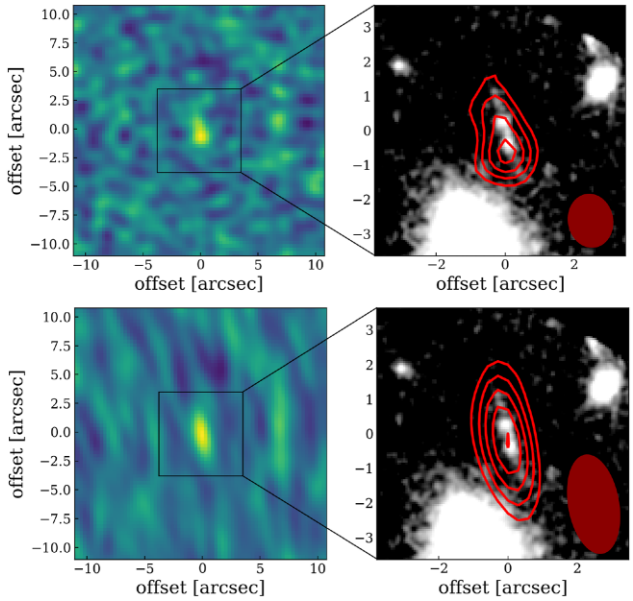


Figure 1. The detection of [C II] at $z = 6.827$ in A1703-zD1. The left-hand panels show the NOEMA + PdBI data collapsed over the frequency range 242.76–242.86 GHz for the untapered (top panels) and tapered (bottom panels) imaging. The right-hand panels show *HST* H_{160} imaging (grey-scale image) overlaid with the 2σ, 3σ, 4σ, 5σ, and 6σ contours of the [C II] narrow-band (red contours). The filled ellipses in the bottom right-hand corner indicate the beam sizes (1.57 × 1.31 arcsec^2 and 2.88 × 1.48 arcsec^2).

Observations for both of these targets covered the same frequency and redshift range. LSB coverage was 240.4–248.3 GHz, corresponding to redshift of 6.66–6.91 and USB coverage was 255.8–263.7 GHz, corresponding to redshift of 6.21–6.43. The coverage described here is shown alongside the SED in Appendix A.

All of the data were reduced using the GILDAS software. From the NOEMA data of A1703-zD1 alone, we obtain a data cube with a median rms of 0.87 mJy in a 40 km s^{-1} channel, with a beam size of 1.52 × 1.28 arcsec^2. After merging with PdBI data (Schaerer et al. 2015) we obtain a data cube with a median rms of 0.83 mJy in a 40 km s^{-1} channel, with a beam size of 1.57 × 1.31 arcsec^2 (∼2 times lower sensitivity than ALMA observations in Smit et al. 2018). We then tapered the data cube for A1703-zD1 such that the beam size matched the spatial extent of the source in the *HST* imaging using a 50 m taper at a 170° angle, in order to obtain a more accurate measurement of the total flux. We also cleaned the data with 100 iterations before imaging the data cube, including a threshold of 0.85 mJy (2 × rms) to reduce the effects of contamination from a strong CO(3–2) emission line signal observed from a serendipitous source. This leads to a median rms in the data cube of 0.73 mJy in a 40 km s^{-1} channel, with a beam size of 2.88 × 1.48 arcsec^2.

We imaged the two Extended Groth Strip (EGS) data cubes with natural weighting for optimal point source sensitivity, resulting in a beam size of 1.69 × 1.41 arcsec^2 and 1.63 × 1.37 arcsec^2 for EGS-5711 and EGS-1952, respectively. Our data reached a typical rms of 0.34 and 0.41 mJy in a 40 km s^{-1} channel, respectively. We do not apply any tapering as our beam sizes are expected to cover any observable [C II] emission from these compact targets (Carniani et al. 2020).

We also produced continuum images using GILDAS for all three targets to provide constraints on the dust obscured star formation and on the dust content itself. For all three targets we merged the USB and LSB before making the continuum images. In the case of A1703-zD1 we removed the frequency range in which [C II] was detected in the corresponding side band. We find no continuum detections above 3σ within 1 arcsec of each source and therefore provide upper limits for the $L_{\rm IR}$ and SFR$_{\rm IR}$, presented in Table 2. These upper limits are derived by taking 3 × rms from the continuum image. Discussion about the significance of these continuum measurements can be found in Section 4.2.

Table 2. Galaxy properties.

Target ID	A1703-zD1	EGS-5711	EGS-1952
$z_{\rm [C\,II]}$	6.8269 ± 0.0004	–	–
Signal-to-noise ratio (S/N)	6.1	–	–
[C II] flux (Jy km s^{-1})	0.28 ± 0.06	$<0.17^a$	$<0.21^a$
FWHM$_{\rm [C\,II]}$ (km s^{-1})	155 ± 31	–	–
Continuum flux (μJy)	$<24.5^a$	$<27.4^a$	$<28.7^a$
$L_{\rm [C\,II]}$ (10^8 L$_\odot$)	$0.35 \pm 0.07\ (^{+0.29}_{-0.04})^c$	$<1.8^a$	$<2.3^a$
SFR$_{\rm [C\,II]}$ (M$_\odot$ yr^{-1})	$4.3 \pm 0.9\ (^{+0.29}_{-0.04})^c$	$<23.9^a$	$<29.5^a$
$L_{\rm UV}$ (10^{11} L$_\odot$)	$0.39 \pm 0.04\ (^{+0.41}_{-0.04})^c$	1.2 ± 0.1	1.0 ± 0.1
SFR$_{\rm UV}$ (M$_\odot$ yr^{-1})	$6.7 \pm 0.6\ (^{+6.41}_{-0.61})^c$	20.2 ± 1.9	17.9 ± 1.7
$L_{\rm IR}$ (10^{11} L$_\odot$)	$<0.35\ (<0.68)^{a,b,c}$	$<3.6^{a,b}$	$<3.9^{a,b}$
SFR$_{\rm IR}$ (M$_\odot$ yr^{-1})	$<5.2\ (<10.1)^{a,b,c}$	$<53.2^{a,b}$	$<57.7^{a,b}$
log(IRX)	$<-0.05^a$	$<0.48^a$	$<0.57^a$

[a] 3σ upper limits.
[b] Assuming a grey body approximation with $T = 50$ K and $\beta = 1.5$.
[c] Corrected for a magnification of $\mu = 9.0$ (the uncertainty due to the lensing magnification are also shown in brackets). Observed quantities are uncorrected for magnification, while the derived physical properties use the magnification correction.

We correct for any offset in the *HST* astrometry by identifying the closest star to the target galaxy in the *Gaia* Data Release 3 (DR3). For EGS-5711 and EGS-1952 the observations were taken ∼4 yr apart and we correct for the proper motion of the star during that time frame, before shifting our *HST* image to the *Gaia* reference star. Unfortunately for A1703-zD1, none of the stars present in the *HST* image had proper motion data from *Gaia* DR3 as a result of being too faint (G magnitudes > 21). Given that the *HST* imaging for Abell 1703 was taken in 2004 (>10 yr apart from *Gaia*), and assuming a similar proper motion to the stars in the EGS field, we expect a ∼0.3 arcsec offset from the reported *Gaia* DR3 position due to proper motion. This angular distance is similar to the typical spatial offset found for the stars in the Abell 1703 field between the *HST* imaging and *Gaia* DR3 catalogue. As a result, no improvement in the astrometry of A1703-zD1 could be obtained and we relied on the original *HST* imaging (see Bradley et al. 2012), but note that a maximum 0.3 arcsec astrometrical offset between the *HST* and NOEMA data is possible. However, we point out that the morphology and size of the [C II] emission for A1703-zD1 match well to the *HST* image, as shown in Fig. 1, so any real offset is perhaps likely to be small. Further, the detection of a serendipitous source with much higher signal-to-noise ratio (S/N) is also present and is seen to be cospatial with the host galaxy as shown in Fig. D2.

3 LINE SCANS

Using the data cubes we obtain after processing, we scan for prominent lines by collapsing channels in the range of 80–400 km s^{-1} (the range of expected [C II] linewidths). This optimizes the width of the collapsed narrow-band for which the strongest point-source signal within a 1 arcsec radius of the target source (identified in the *HST* imaging) is found, if any. Scanning through the data cube also enables us to identify any lines present from serendipitous sources.

Downloaded from https://academic.oup.com/mnras/article/512/1/535/6542457 by guest on 19 March 2023

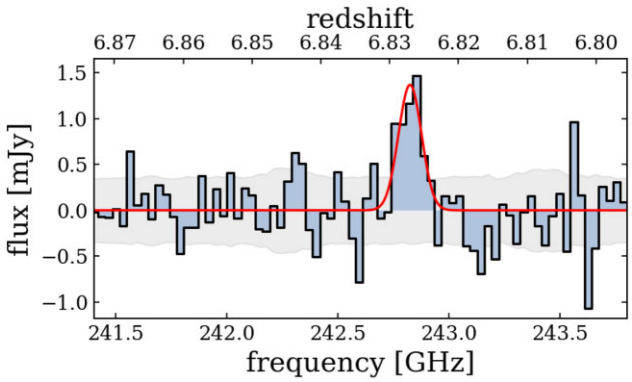


Figure 2. The spectrum of A1703-zD1 extracted by summing the flux over the source from all pixels with S/N > 2, using the tapered imaging. The red line shows the best-fitting Gaussian line profile. The grey shaded region gives the measured rms throughout the spectrum.

We replicate this scanning in the sign-inverse of the data cube, to check if any noise is comparable to the signal detected from the target source and assess the robustness of any tentative ($>3\sigma$) line detections. We extract spectra from identified line candidates by summing all pixels detected at S/N > 2 in the collapsed narrow-band.

3.1 A1703-zD1

Taking our NOEMA observations of A1703-zD1 in isolation we find a signal at 242.90 ± 0.01 GHz with S/N = 4.6, cospatial with the lower bright clump and extended along the lensed arc, visible in *HST* imaging (see Fig. 1). From previous observations by Schaerer et al. (2015), we independently identified a tentative detection of [C II] with S/N = 3.4 at 242.853 ± 0.009 GHz. The top panel of Fig. 1 presents the line detection after combining both data sets (see Section 2.2), collapsed in a 120 km s^{-1} channel centred on 242.8 GHz, with a peak S/N of 5.5. To obtain an unresolved measurement of A1703-zD1 we taper the data cube to match the spatial extent of A1703-zD1 (described in Section 2.2). From this we find a detection at 242.82 ± 0.01 GHz with an increase in the peak S/N to 6.1, yielding a best-fitting $z_{[\mathrm{C\,II}]}$= 6.8269 ± 0.0004 from the extracted spectrum (see Fig. 2). This higher S/N when matching the spatial extent of the target (and alignment with the rest-frame UV emission) is a clear confirmation of the detection. We therefore use the tapered imaging for our final measurements. We collapse the data cube over the frequency range 242.72–242.92 GHz and measure the total flux using 2D Gaussian fitting from the routine IMFIT in the Common Astronomy Software Application (CASA; McMullin et al. 2007).

We also note that within the same data cube, we identify a serendipitous line signal at 241.59 GHz with S/N ∼ 14 (see spectrum in Fig. D1), ∼8 arcsec offset to A1703-zD1. The signal is cospatial with a foreground source (J131459.75+515008.6) that has z_{phot} ∼ 0.44 ± 0.11 [found in Sloan Digital Sky Survey Data Release 12 (SDSS DR12); Alam et al. 2015]. We therefore identify the line as CO(3–2) (rest-frame wavelength 867 μm) at $z_{\mathrm{spec}} = 0.43127 \pm 0.00003$, consistent with the z_{phot}. We also measure a 68 μJy continuum flux from this source with S/N of 5.1.

3.2 EGS-5711 and EGS-1952

When scanning for [C II] in EGS-5711 we find a tentative signal with S/N = 4.6 at 246.16 ± 0.02 GHz, 0.5 arcsec away from the centre of the target. This line, if real, would put the source at z = 6.7263 ± 0.0006. A second signal at 242.10 ± 0.03 GHz with S/N = 3.4 is also found cospatial with EGS-5711. The corresponding spectra and contour overlay plots for the S/N = 4.6 signal can be found in Appendix B (Figs B1 and B2). In Figs C1 and C2 in Appendix C, we also present the spectra at the location of the source to illustrate the lack of detection there. Performing the same scan on the inverse data cube (searching within a radius of 15 arcsec), we find several signals with equivalent or higher S/N, the highest of which is S/N = 5.3. Given our 15 times larger search area, we expect ∼1 spurious signal above 4.5σ within 1 arcsec radius of our target. More observations are therefore required to confirm any detection.

For EGS-1952 we find no evidence for [C II] with S/N > 3, cospatial with the source. Spectra at the location of the source can be found in Appendix C (Figs C3 and C4). Further, we find no continuum signal for both EGS-5711 and EGS-1952 and as a result, we only provide upper limits for the continuum flux and an upper limit estimate for the [C II] line flux, based on the spectral line obtained for A1703-zD1, scaled to the median rms of the EGS-5711 and EGS-1952 data cubes.

We can either interpret these non-detections as faint [C II] lines due to the low dust content of these sources or alternatively it is possible that the limited frequency range that was scanned for each object missed the line emission entirely. Deeper and wider scans would be needed to distinguish between these two interpretations (see Appendix A).

4 SOURCE PROPERTIES

Here we present the physical properties of our three targets derived from our observations and comparisons to the literature. A full table of galaxy properties is shown in Table 2.

4.1 $L_{[\mathrm{C\,II}]}$ versus SFR relation

In Fig. 3, we present the measured [C II] luminosity as a function of $\mathrm{SFR_{UV}}$ and include sources from the literature for comparison (Knudsen et al. 2016; Bradač et al. 2017; Matthee et al. 2019; Fujimoto et al. 2021). The UV SFRs are calculated using the Kennicutt & Evans (2012) conversion, using a Kroupa IMF. EGS-5711 and EGS-1952 are given as 3σ upper limits.

In the local Universe we see a tight $L_{[\mathrm{C\,II}]}$–SFR relationship as shown by the De Looze et al. (2014) relation ($\log \mathrm{SFR} = -6.99 + 1.01 \times \log[\mathrm{C\,II}]$) in Fig. 3. Recent studies of 'normal' (i.e. main sequence) star-forming galaxies with redshifts at $4.4 < z < 5.9$ and galaxies at $z \sim 6.5$ with high Lyα luminosities have also shown consistency with the local relation when including the dust-obscured SFR (e.g. Matthee et al. 2019; Schaerer et al. 2020). In contrast, a few studies have found that lensed galaxies with a lower SFR are more likely to be below the locally observed relation (e.g. Knudsen et al. 2016; Bradač et al. 2017). In particularly the strongest lensed object, MS0451-H (Knudsen et al. 2016), with the lowest intrinsic SFR shows the strongest deficit in $L_{[\mathrm{C\,II}]}$. If confirmed, this could suggest differing ISM properties in faint, and possibly more metal-poor, high-redshift galaxies. A1703-zD1 is a strongly lensed galaxy with a modest intrinsic $\mathrm{SFR_{UV}}$ of 6.7 ± 0.6 $\mathrm{M_\odot\ yr^{-1}}$, but we find no evidence of a significant offset to the local relation, as A1703-zD1 lies slightly below, but still within 1σ, the local $L_{[\mathrm{C\,II}]}$–SFR relation. We also note that including the magnification uncertainties in the calculations of $L_{[\mathrm{C\,II}]}$ and $\mathrm{SFR}_{[\mathrm{C\,II}]}$ has no impact on the offset to the local relation as indicated by the arrows in Fig. 3. However, including the 3σ upper limit on the $\mathrm{SFR_{IR}}$ would place A1703-zD1 below the local relation.

Downloaded from https://academic.oup.com/mnras/article/512/1/535/6542457 by guest on 19 March 2023

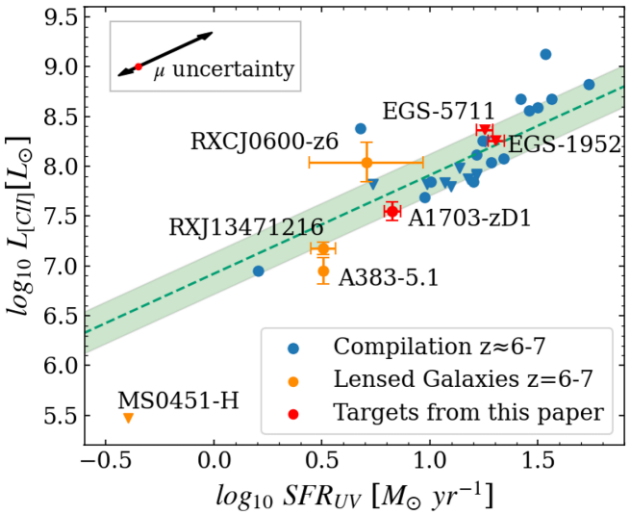


Figure 3. The [C II] line luminosity as a function of the star formation rate (SFR), derived from the ultraviolet (UV) luminosity. The locally observed De Looze et al. (2014) relation is indicated by the dotted green line with the errors shown by the green shaded region. Sources with 3σ upper limits are shown by downward triangles. Our three targets are presented as red points. The black arrows in the top-left indicate the magnification uncertainty for A1703-zD1. Changes in magnification affect both $L_{[C\,II]}$ and SFR_{UV}, such that A1703-zD1 moves along the local relation. We use a compilation of $z \approx$ 6–7 sources for comparison (compiled from Matthee et al. 2019), shown in blue. In orange we highlight four lensed sources from the literature (Knudsen et al. 2016; Bradač et al. 2017; Fujimoto et al. 2021) for which three show an apparent offset from the local $L_{[C\,II]}$–SFR relation, one of which shows a very clear offset (MS0451-H, discussed more in Section 4.1).

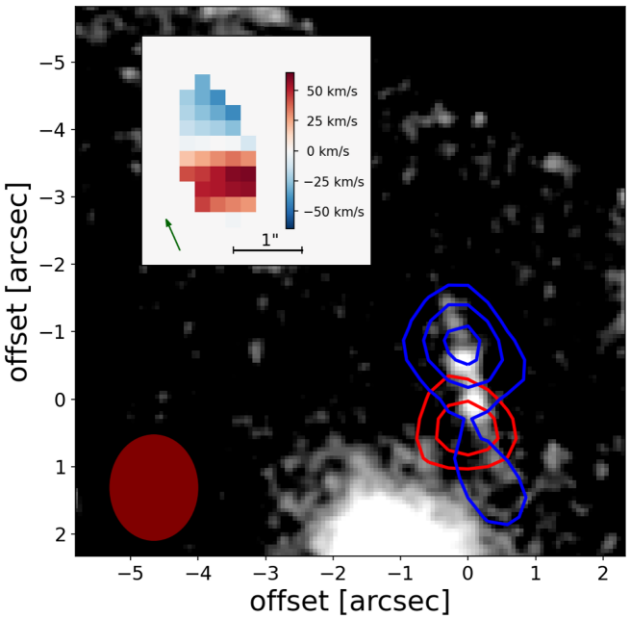


Figure 4. Main panel: *HST* imaging overlaid with contours from the untapered data cube corresponding to 2σ, 3σ, and 4σ [C II] emission collapsed over channels redwards (red contours) and bluewards (blue contours) of the measured line centre, showing evidence for a velocity gradient. The observations are spatially resolved, as shown by the filled ellipse indicating the beam size (1.57×1.31 arcsec^2). Inset panel: first moment map of the detected [C II] from A1703-zD1 (showing pixels above 2σ). We measure a velocity difference over the galaxy of 103 ± 22 km s^{-1}. We show the green arrow to illustrate the stretching of the arc in the image plane with respect to the source-plane image of this source.

An important consideration in assessing a possible [C II] deficit is the potential for extended [C II] emission (e.g. Fujimoto et al. 2019, 2020) compared to the rest-frame UV data, in particular for sources with smearing due to strong gravitational lensing. This effect was recently studied by Carniani et al. (2020), who find that [C II] emission can be two times more extended than [O III]. Specifically, Carniani et al. (2020) show that MS0451-H (Knudsen et al. 2016), nominally a 2.5σ deviation from the local De Looze relation (Fig. 3), misses ∼60–80 per cent of the [C II] emission if the effects of lensing are ignored. Taking into account possible extended [C II] moves MS0451-H to within 1σ of the local relation.

In A1703-zD1, we aim to account for lens smearing by tapering the data cube to match the spatial extent of A1703-zD1 in the *HST* imaging, allowing us to obtain a more accurate flux measurement. Without tapering and using the same routine as described in Section 3.1, we calculate a [C II] integrated flux value that is 51 per cent of our fiducial measurement. However, extended [C II] beyond the rest-frame UV could still be missed even with our current tapering strategy, consistent with Carniani et al. (2020).

4.2 L_{IR} and SFR_{IR} constraints

As discussed in Section 2.2, the continuum flux remains undetected for all our sources. We calculate upper limits for L_{IR} and SFR_{IR} by assuming an optically thin grey-body infrared SED (Casey 2012) using $T = 50$ K and $\beta = 1.5$, and present the results in Table 2. We estimate that these sources are likely below the classification of luminous infrared galaxies (LIRGs; $L_{IR} > 10^{11}$ L$_\odot$). We furthermore find obscured SFR below 5–58 M$_\odot$ yr^{-1} (3σ limits), which suggests less than 44–74 per cent of star formation comes out in the infrared (IR), consistent with recent studies (e.g. Bowler et al. 2018; Schouws et al. 2021).

We derive UV slopes (β) and upper limits on the infrared excess ($IRX = L_{IR}/L_{UV}$) for all our targets (see Tables 1 and 2) and find that the upper limits for EGS-5711 and EGS-1952 are consistent with either the Meurer, Heckman & Calzetti (1999) relation or a Small Magellanic Cloud (SMC)-like dust attenuation.

However, given a moderately red UV slope for A1703-zD1 of $\beta \sim -1.56$, we find this galaxy to be more consistent with an SMC-like dust attenuation law, in agreement with stacking results of faint Lyman-break galaxies at $z \approx$ 2–10 (Bouwens et al. 2016; Fudamoto et al. 2020, though see Schouws et al. 2021 for a discussion on the impact of the assumed dust temperature).

4.3 Velocity structure

We use the spatial extent of the [C II] detection to investigate the velocity structure of A1703-zD1. We see a velocity gradient across A1703-zD1 shown in Fig. 4. We find a maximum projected velocity difference over the galaxy (Δv_{obs}) of 103 ± 22 km s^{-1} from the first moment map. Such a velocity gradient could be the signature of a rotating disc, whilst another possibility is a merger of [C II] emitting galaxies. Similar velocity gradients are present in previous observations of high-redshift galaxies (e.g. Smit et al. 2018; Hashimoto et al. 2019; Matthee et al. 2019; Fujimoto et al. 2021) and in simulations (Dekel & Burkert 2014).

To determine the likelihood of a disc-like rotation we compare the projected velocity range of a galaxy with the velocity dispersion of the system using $\Delta v_{obs}/2\sigma_{tot}$, where a ratio of >0.4 indicates

Downloaded from https://academic.oup.com/mnras/article/512/1/535/6542457 by guest on 19 March 2023

a likely rotation-dominated system (Förster Schreiber et al. 2009). We find $\Delta v_{\rm obs}/2\sigma_{\rm tot} = 0.79 \pm 0.23$ for A1703-zD1, which supports the interpretation of a possibly rotation-dominated system. Bradley et al. (2012) find three distinct star-forming clumps with an extended linear morphology in the source-plane reconstruction of A1703-zD1. In Fig. 4, we show the deflection due to the lensing magnification, using the LTM strong-lensing model published by Zitrin et al. (2010). This stretching of the source-plane leads to an effective increase in resolution of 3.5×, in the direction of the green arrow shown in Fig. 4. The red and blue components identified in Fig. 4 appear cospatial with the two brightest clumps from Bradley et al. (2012). Clumps like this have been identified previously in high-redshift galaxies and can be attributed to merging galaxies or large clumpy star formation due to the increased gas content in high-redshift galaxies. Higher resolution [C II] observations will be required to confirm a disc-like structure in A1703-zD1.

If we assume ordered circular rotation we can use the full width at half-maximum (FWHM) of [C II] to estimate the dynamical mass. We use $M_{\rm dyn} = 1.16 \times 10^5 V_{\rm cir}^2 D$ (Capak et al. 2015), where $V_{\rm cir} = 1.763 \times \sigma_{\rm [C\,II]}/\sin i$ in km s^{-1}, i is the disc inclination angle, and D is the disc diameter in kpc (we use $D = 4$ kpc found in Bradley et al. 2012; measured in the reconstructed sources-plane image). Assuming a viewing angle of 45° we find $M_{\rm dyn} = 12.1 \pm 4.8 \times 10^9$ M$_\odot$. The stellar mass of A1703-zD1 was estimated to be $0.7 \pm 0.1 \times 10^9$ M$_\odot$ (Bradley et al. 2012). This stellar mass is only ∼6 per cent of the total dynamical mass that we measure. This is somewhat low compared to dynamical measurements from Hα surveys at cosmic noon; for example, Stott et al. (2016) find a value of 22 ± 11 per cent in a sample of 584 $z \sim 1$ galaxies and Wuyts et al. (2016) find a value of 32^{+8}_{-7} per cent in star-forming galaxies $0.6 < z < 2.6$. Larger and more detailed samples of dynamical measurements at $z \sim 7$ will be needed to establish evolutionary trends with redshift. We also note that there are large uncertainties on the dynamical mass, as there is a large dependency on the viewing angle (which is unknown). However, this low ratio does suggest that A1703-zD1 is a gas-rich system, similar to typical star-forming galaxies 3 Gyr later in cosmic time.

5 SUMMARY AND CONCLUSIONS

We have presented new NOEMA observations, scanning for the [C II] 158 μm line in three Lyman-break galaxies with photometric redshifts at $z = 6.6$–6.9. Our main findings are as follows.

(i) We detect [C II] in one of our three sources, confirming the redshift at $z = 6.8269 \pm 0.0004$ for the strongly lensed galaxy A1703-zD1 (6.1σ). Our non-detections are consistent with these being dust-poor galaxies with low [C II] luminosity.

(ii) We carefully account for any extended emission of [C II] due to lens smearing in A1703-zD1 and find the [C II] luminosity to be consistent with, but slightly below, the local $L_{\rm [C\,II]}$–SFR relation.

(iii) No continuum emission is detected in any of the three targeted sources, suggesting less than 44–74 per cent of star formation comes out in the IR. For A1703-zD1, our results are most consistent with an SMC attenuation curve.

(iv) We see a velocity gradient across A1703-zD1, with a kinematic ratio that suggests a possible rotation-dominated system, though higher resolution [C II] observations will be needed to confirm this.

Over the last few years ALMA has demonstrated its role as a 'redshift machine' in the EoR by confirming galaxies out to redshift $z = 9$. In this paper, we have demonstrated the ability of NOEMA to search for [C II] in 'normal' star-forming galaxies at $z > 6$, complementing ALMA by observing EoR galaxies in the Northern hemisphere, with [C II] as a reliable spectroscopic tracer of these distant systems. With the launch of the *James Webb Space Telescope* (*JWST*) this capability will be particularly useful for rare, lensed sources and intrinsically luminous objects that will be discovered far outside the limited *JWST* survey area using the next generation of large area surveys, such as the *Euclid* mission and the Rubin Observatory.

ACKNOWLEDGEMENTS

We thank the anonymous referee for constructive feedback and useful suggestions. RS acknowledges support from an STFC Ernest Rutherford Fellowship (ST/S004831/1). AZ acknowledges support by Grant No. 2020750 from the United States-Israel Binational Science Foundation (BSF) and Grant No. 2109066 from the United States National Science Foundation (NSF), and by the Ministry of Science and Technology, Israel. JAH gratefully acknowledges support of the VIDI research program with project number 639.042.611, which is (partly) financed by the Netherlands Organisation for Scientific Research (NWO).

DATA AVAILABILITY

The reduced data underlying this paper will be shared on reasonable request to the corresponding author.

REFERENCES

Alam S. et al., 2015, ApJS, 219, 12
Bakx T. J. L. C. et al., 2020, MNRAS, 493, 4294
Béthermin M. et al., 2020, A&A, 643, A2
Bouwens R. J. et al., 2016, ApJ, 833, 72
Bouwens R. J., Illingworth G. D., van Dokkum P. G., Ribeiro B., Oesch P. A., Stefanon M., 2021, AJ, 162, 255
Bowler R. A. A., Bourne N., Dunlop J. S., McLure R. J., McLeod D. J., 2018, MNRAS, 481, 1631
Bradač M. et al., 2017, ApJ, 836, L2
Bradley L. D. et al., 2012, ApJ, 747, 3
Brammer G. B., van Dokkum P. G., Coppi P., 2008, ApJ, 686, 1503
Capak P. L. et al., 2015, Nature, 522, 455
Carniani S. et al., 2017, A&A, 605, A42
Carniani S. et al., 2020, MNRAS, 499, 5136
Casey C. M., 2012, MNRAS, 425, 3094
Dekel A., Burkert A., 2014, MNRAS, 438, 1870
De Looze I. et al., 2014, A&A, 568, A62
Endsley R., Stark D. P., Charlot S., Chevallard J., Robertson B., Bouwens R. J., Stefanon M., 2021, MNRAS, 502, 6044
Förster Schreiber N. M. et al., 2009, ApJ, 706, 1364
Fudamoto Y. et al., 2020, A&A, 643, A4
Fujimoto S. et al., 2019, ApJ, 887, 107
Fujimoto S. et al., 2020, ApJ, 900, 1
Fujimoto S. et al., 2021, ApJ, 911, 99
Ginolfi M. et al., 2020, A&A, 633, A90
Harikane Y. et al., 2019, ApJ, 883, 142
Hashimoto T. et al., 2018, Nature, 557, 392
Hashimoto T., Inoue A. K., Tamura Y., Matsuo H., Mawatari K., Yamaguchi Y., 2019, PASJ, 71, 109
Hodge J. A., da Cunha E., 2020, R. Soc. Open Sci., 7, 200556
Inoue A. K. et al., 2016, Science, 352, 1559
Jung I. et al., 2020, ApJ, 904, 144
Kennicutt R. C., Evans N. J., 2012, ARA&A, 50, 531
Knudsen K. K., Richard J., Kneib J.-P., Jauzac M., Clément B., Drouart G., Egami E., Lindroos L., 2016, MNRAS, 462, L6
Kroupa P., 2001, MNRAS, 322, 231

Downloaded from https://academic.oup.com/mnras/article/512/1/535/6542457 by guest on 19 March 2023

Laporte N., Nakajima K., Ellis R. S., Zitrin A., Stark D. P., Mainali R., Roberts-Borsani G. W., 2017, ApJ, 851, 40
Laporte N. et al., 2021, MNRAS, 505, 4838
McMullin J. P., Waters B., Schiebel D., Young W., Golap K., 2007, in Shaw R. A., Hill F., Bell D. J., eds, ASP Conf. Ser. Vol. 376, Astronomical Data Analysis Software and Systems XVI. Astron. Soc. Pac., San Francisco, p. 127
Mainali R. et al., 2018, MNRAS, 479, 1180
Maiolino R. et al., 2015, MNRAS, 452, 54
Matthee J. et al., 2019, ApJ, 881, 124
Meurer G. R., Heckman T. M., Calzetti D., 1999, ApJ, 521, 64
Oke J. B., Gunn J. E., 1983, ApJ, 266, 713
Schaerer D., Boone F., Zamojski M., Staguhn J., Dessauges-Zavadsky M., Finkelstein S., Combes F., 2015, A&A, 574, A19
Schaerer D. et al., 2020, A&A, 643, A3
Schenker M. A., Stark D. P., Ellis R. S., Robertson B. E., Dunlop J. S., McLure R. J., Kneib J.-P., Richard J., 2012, ApJ, 744, 179
Schouws S. et al., 2021, preprint (arXiv:2105.12133)
Schuster K. F. et al., 2018, in Marshall H. K., Spyromilio J., eds, Proc. SPIE Vol. 10700, Ground-based and Airborne Telescopes VII. SPIE, Bellingham, p. 107000R
Smit R. et al., 2014, ApJ, 784, 58
Smit R. et al., 2015, ApJ, 801, 122
Smit R. et al., 2018, Nature, 553, 178
Stark D. P., 2016, ARA&A, 54, 761
Stark D. P. et al., 2015, MNRAS, 454, 1393
Stott J. P. et al., 2016, MNRAS, 457, 1888
Tamura Y. et al., 2019, ApJ, 874, 27
Watson D., Christensen L., Knudsen K. K., Richard J., Gallazzi A., Michałowski M. J., 2015, Nature, 519, 327
Willott C. J., Carilli C. L., Wagg J., Wang R., 2015, ApJ, 807, 180
Wuyts S. et al., 2016, ApJ, 831, 149
Zitrin A. et al., 2010, MNRAS, 408, 916

APPENDIX A: PHOTOMETRIC REDSHIFT COVERAGE

Here we present the SEDs for all three targets in this paper, alongside the photometric redshift probability distributions, redshift coverage of the observations, and in the case of A1703-zD1, the measured $z_{[\mathrm{C\,II}]}$ (Figs A1–A3). The SED fitting was done using the software Easy and Accurate Zphot from Yale (EAZY; Brammer, van Dokkum & Coppi 2008); see Smit et al. (2015) for a full description.

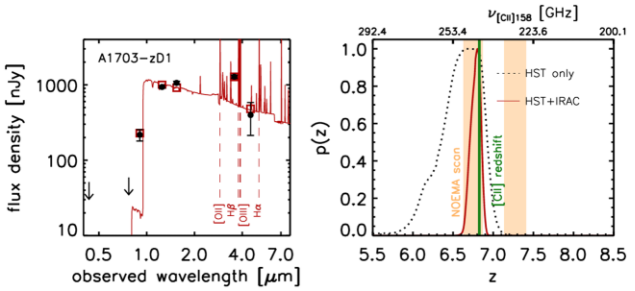


Figure A1. A1703-zD1 SED (left-hand panel) and redshift probability distribution (right-hand panel). Coverage by the NOEMA sidebands (USB and LSB) is indicated by the shaded orange region. The dotted black line and solid red line represent the probability for the target to be at a certain redshift based on *HST* only and *HST* + IRAC data, respectively. Here the USB was selected to cover the peak probability in the photometric redshift range, which is indeed where the detection of [C II] was made, indicated by the solid green line.

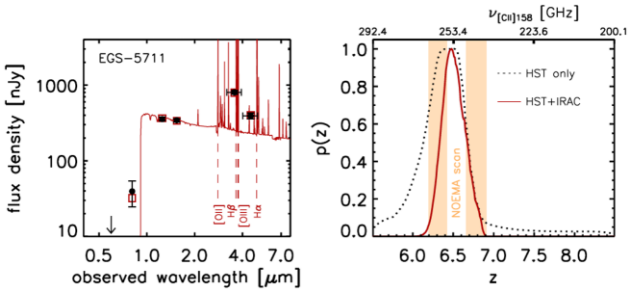


Figure A2. EGS-5711 SED (left-hand panel) and redshift probability distribution (right-hand panel). Coverage by the NOEMA sidebands (USB and LSB) is indicated by the shaded orange region. The dotted black line and solid red line represent the probability for the target to be at a certain redshift based on *HST* only and *HST* + IRAC data, respectively. This target was selected to be at $z \sim 6.6$–6.9 based on *HST* + IRAC data colour criteria (Smit et al. 2015), however, the peak of the $p(z)$ suggests a possible lower redshift. A broader and deeper line scan will be needed to establish the spectroscopic redshift of this source.

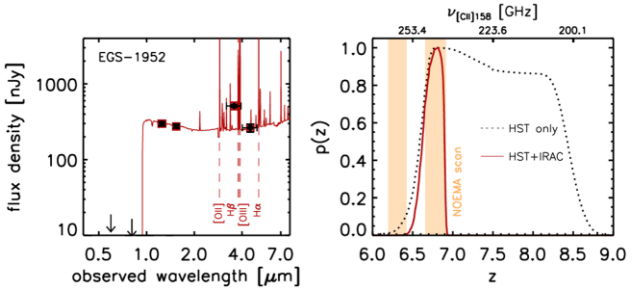


Figure A3. EGS-1952 SED (left-hand panel) and redshift probability distribution (right-hand panel). Coverage by the NOEMA sidebands (USB and LSB) is indicated by the shaded orange region. The dotted black line and solid red line represent the probability for the target to be at a certain redshift based on *HST* only and *HST* + IRAC data, respectively.

We note that for EGS-5711, NOEMA did not cover the central z_{phot} of $6.47^{+0.11}_{-0.10}$. The systematic uncertainties in estimating photometric redshifts in extreme emission line galaxies are discussed in Section 2.1, which motivated a line search at $z \sim 6.6$–6.9 based on the Smit et al. (2015) colour selection.

APPENDIX B: EGS-5711 TENTATIVE DETECTION

Here we present a 4.6σ signal for EGS-5711, with the contours overlaid on the *HST* imaging in Fig. B1 and the corresponding spectra in Fig. B2. The spectral extraction is the same as described in Section 3. The weak signal is very narrow and clearly offset from the *HST* target, which likely makes this a spurious detection.

Downloaded from https://academic.oup.com/mnras/article/512/1/535/6542457 by guest on 19 March 2023

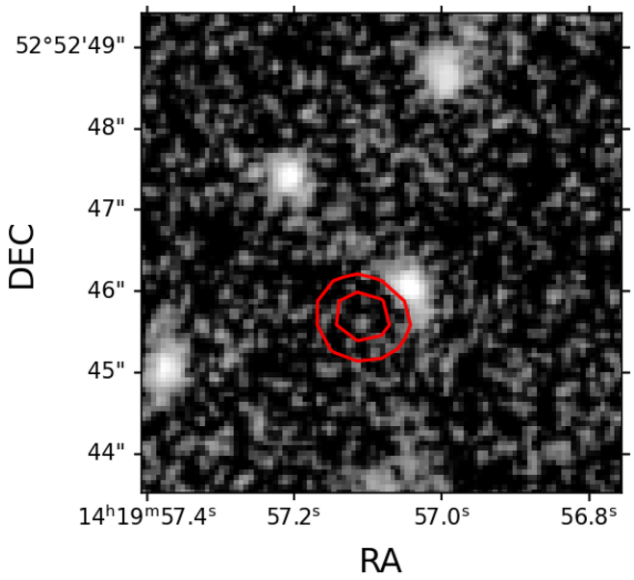


Figure B1. The S/N = 4.6 signal found for EGS-5711. Background shows the *HST H*-band image with red contours corresponding to 3σ and 4σ [C II] emission. The extracted spectrum is also shown in Fig. B2. This source would require further observations to confirm a robust detection.

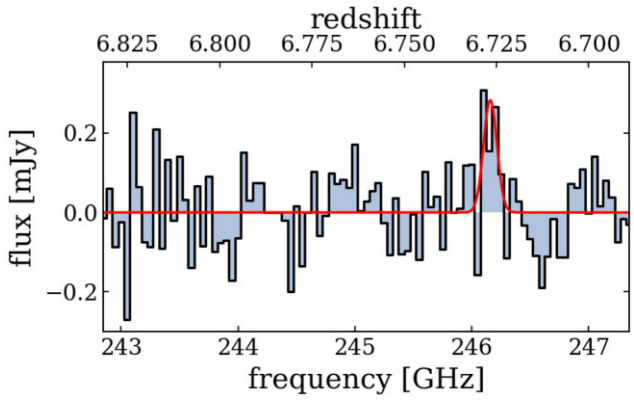


Figure B2. EGS-5711 spectrum of the S/N = 4.6 signal, extracted from the region of the contours shown in Fig. B1, with the best-fitting Gaussian line profile in red.

APPENDIX C: EMPTY SCANS

In Figs C1–C4, we present the empty line scans in the LSB and USB for both EGS targets. The extractions were taken simply from the central pixel of the observations.

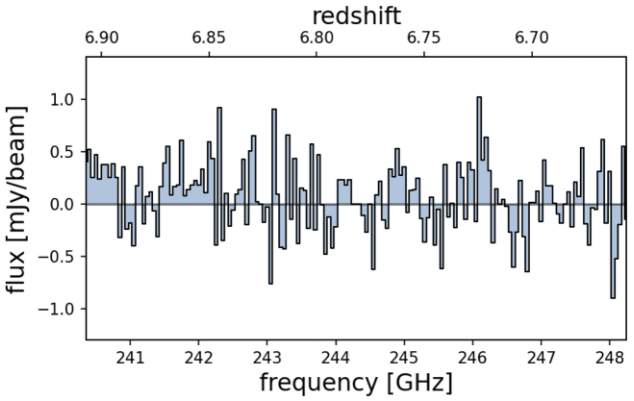


Figure C1. LSB spectra taken at the location of EGS-5711. We find no robust detection and present upper limits in Table 2.

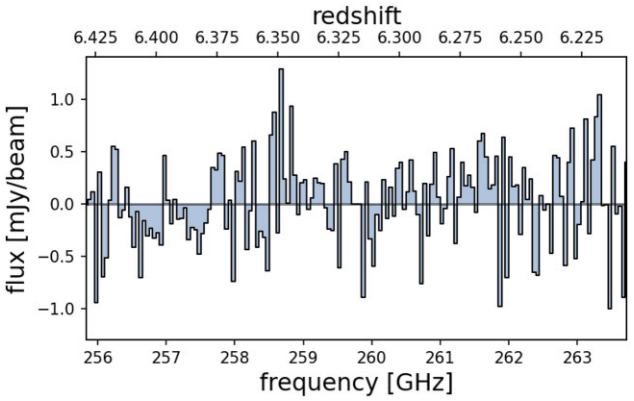


Figure C2. USB spectra taken at the location of EGS-5711.

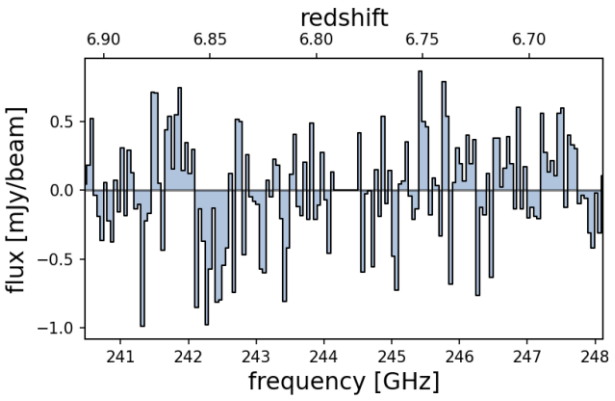


Figure C3. LSB spectra taken at the location of EGS-1952. We find no detection and present upper limits in Table 2.

Downloaded from https://academic.oup.com/mnras/article/512/1/535/6542457 by guest on 19 March 2023

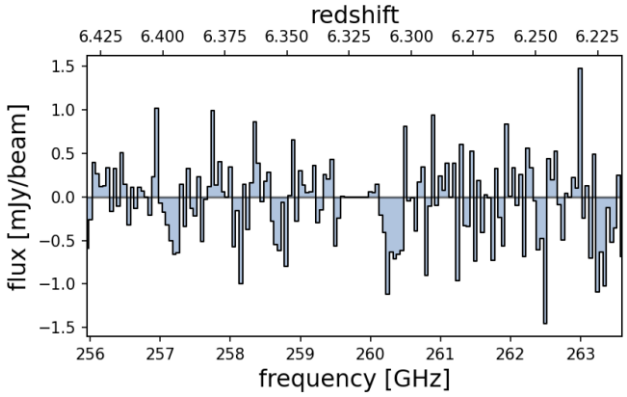


Figure C4. USB spectra taken at the location of EGS-1952.

APPENDIX D: SERENDIPITOUS SOURCE IN A1703-ZD1 CUBE

Here we present a serendipitous 14σ detection in the data cube of A1703-zD1, with the spectra shown in Fig. D1 and the line contours overlaid on the *HST* imaging in Fig. D2. The spectral extraction is the same as described in Section 3. The detection is cospatial with a foreground source (J131459.75+515008.6) that has $z_{\rm phot} \sim 0.44 \pm 0.11$ (found in SDSS DR12; Alam et al. 2015). We therefore attribute the line detection to CO(3–2) (rest-frame wavelength 867 μm) putting the source at $z_{\rm spec} = 0.43127 \pm 0.00003$, consistent with the $z_{\rm phot}$.

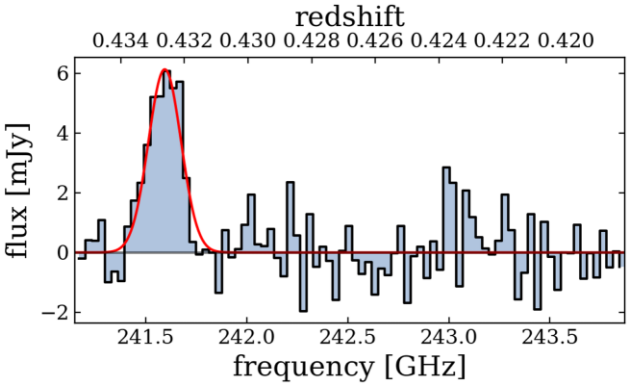


Figure D1. Spectrum of the serendipitous line identified in the data cube of A1703-zD1, with the best-fitting Gaussian line profile in red. The redshifts plotted along the upper horizontal axis are based on the assumption the line detection is CO(3–2) for the source J131459.75+515008.6. The S/N of the line is 14.

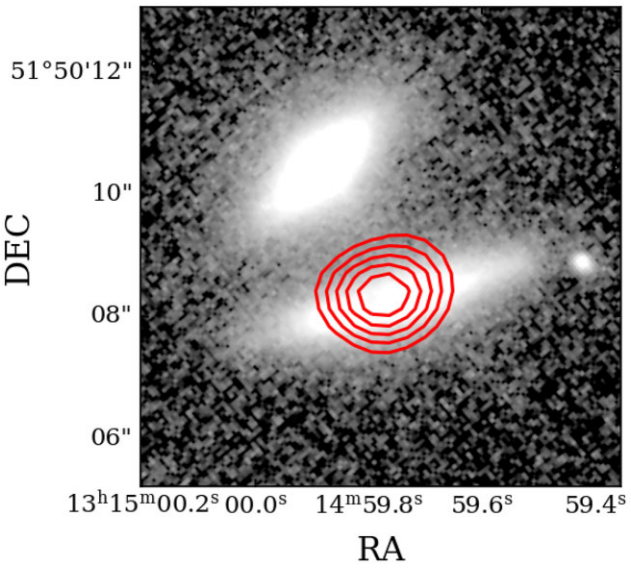


Figure D2. Serendipitous source (J131459.75+515008.6) with red contours overlaid corresponding to 4σ, 6σ, 8σ, 10σ, and 12σ, identified as CO(3–2) emission. Background shows the *HST* z_{850} imaging of Abell 1703.

This paper has been typeset from a TEX/LATEX file prepared by the author.

Downloaded from https://academic.oup.com/mnras/article/512/1/535/6542457 by guest on 19 March 2023